Numerical investigation of dam break flow over erodible beds with diverse substrate level variations

Alireza Khoshkonesh[1], Blaise Nsom[2], Saeid Okhravi[3*], Fariba Ahmadi Dehrashid[4], Payam Heidarian[5], Silvia DiFrancesco[6]

[1] Department of Geography, School of Social Sciences, History, and Philosophy, Birkbeck University of London, London, UK.
[2] Université de Bretagne Occidentale. IRDL/UBO UMR CNRS 6027. Rue de Kergoat, 29285 Brest, France.
[3] Institute of Hydrology, Slovak Academy of Sciences, Dúbravská cesta 9, 84104, Bratislava, Slovak Republic.
[4] Department of Water Science and Engineering, Faculty of Agriculture, Bu-Ali Sina University, 65178-38695, Hamedan, Iran.
[5] Department of Civil, Environmental, Architectural Engineering and Mathematics, University of Brescia, 25123 Brescia, Italy.
[6] Niccol`o Cusano University, via Don C. Gnocchi 3, 00166 Rome, Italy.
* Corresponding author. Tel.: +421-944624921. E-mail: saeid.okhravi@savba.sk

Abstract: This study aimed to comprehensively investigate the influence of substrate level difference and material composition on dam break wave evolution over two different erodible beds. Utilizing the Volume of Fluid (VOF) method, we tracked free surface advection and reproduced wave evolution using experimental data from the literature. For model validation, a comprehensive sensitivity analysis encompassed mesh resolution, turbulence simulation methods, and bed load transport equations. The implementation of Large Eddy Simulation (LES), non-equilibrium sediment flux, and van Rijn's (1984) bed load formula yielded higher accuracy compared to alternative approaches. The findings emphasize the significant effect of substrate level difference and material composition on dam break morphodynamic characteristics. Decreasing substrate level disparity led to reduced flow velocity, wavefront progression, free surface height, substrate erosion, and other pertinent parameters. Initial air entrapment proved substantial at the wavefront, illustrating pronounced air-water interaction along the bottom interface. The Shields parameter experienced a one-third reduction as substrate level difference quadrupled, with the highest near-bed concentration observed at the wavefront. This research provides fresh insights into the complex interplay of factors governing dam break wave propagation and morphological changes, advancing our comprehension of this intricate phenomenon.

Keywords: Dam break; Substrate level difference; Erodible bed; Sediment transport; Computational fluid dynamics CFD.

INTRODUCTION

The morphology of the bed plays a crucial role in influencing the dynamic characteristics of floods that arise from dam failures. It encompasses various aspects such as the bed material, bed elevation, and bed compaction and mobility. These factors collectively contribute to strengthening the retention forces that act against flood propagation (Dehrashid et al., 2023; Issakhov et al., 2018; Kim et al., 2017; Oguzhan, and Aksoy, 2020; Riaz et al., 2022). Understanding the dynamics of dam failure on vulnerable terrains is of paramount importance. This knowledge is instrumental in comprehending the catastrophic flood events triggered by dam failures, a phenomenon with profound implications for sediment transport, scour processes, and flood risk assessment.

The complexity of dam failure flows arises from the interaction of multiple influencing factors (Biscarini et al., 2013). Existing studies have primarily focused on investigating the effects of initial reservoir and tailwater depth (Khoshkonesh et al., 2019; Nsom et al., 2019; Yang et al., 2018), fluid viscosity (Nsom et al., 2008), channel characteristics (Issakhov et al., 2018; Khayyer and Gotoh, 2010; Kocaman and Ozmen-Cagatay, 2012), and reservoir sediment depth called silted-up reservoirs (Gu et al., 2023; Vosoughi et al., 2020). However, none of these studies have examined dam failure above an erodible bed, which includes substrate elevation which is a factor that significantly impacts dam failure wave dynamics.

In a real dam breach, sediment loads originate from three primary sources: the reservoir, downstream channel substrates, and dam material (Baklanov, 2007; Khoshkonesh et al., 2019, 2022). Particularly, the characteristics of the reservoir and downstream substrates play a pivotal role in determining the evolution of waves during a dam failure (Leal et al., 2006; Mei et al., 2022; Xu et al., 2023). However, these studies fail to consider the critical aspect of varying substrate levels at the dam site, which significantly affects the morphodynamic characteristics of the dam breach. The existing research has only touched upon this aspect briefly, emphasizing the necessity for a more comprehensive analysis. Therefore, the present study aims to fill this gap by providing a comprehensive and insightful assessment of the flow dynamics associated with dam breaches over an erodible bed with elevation changes at the dam site, an aspect that has been inadequately addressed in previous research.

The present study aims to investigate the effects of substrate topography on flow and wave dynamics following dam failure, utilizing the advanced Flow-3D CFD package. The researchers provide a detailed numerical analysis of dam break flow over an erodible bed, taking into account the elevation differences in the substrate. The model employs the Volume of Fluid (VOF) method (Hirt and Nichols, 1981) and the Large Eddy Simulation (LES) turbulence closure model, which ensures an accurate representation of flow field characteristics, similar to the studies conducted by Li et al. (2019) and Li and Yu (2019). By employing these state-of-the-art tools and methods, the study

adds a new dimension to existing research and offers a more comprehensive understanding of the flow regime, transverse and vertical velocities, particle Reynolds number, air entrapment, Shields parameter, and suspended sediment concentration resulting from dam break flow over an erodible bed with a height difference at the dam site. This information holds significant practical importance and enhances our ability to manage catastrophic flood events. The pragmatic applications of the present study are of interest to both academic and non-academic sectors, as well as researchers involved in waterway design, flood modelling, and risk analysis in various aquatic environments.

METHODOLOGY
Governing equations

The clear water flow model (i.e. no sediment supply) is governed by a set of equations describing fluid momentum (Eqs. 1–3) for incompressible flow in a Cartesian coordinate system, coupled with the volume of fluid (VOF) advection (Eq. 3). The equation of continuity (Eq. 1) and the Navier-Stokes equation (Eq. 2) are provided below (Flow3D, 2023):

$$\nabla \cdot u = 0 \tag{1}$$

$$\partial u / \partial t + u \cdot \nabla u = \frac{-1}{\rho} \nabla p + \vartheta \nabla^2 u + g + \frac{1}{\rho} f_{st} \tag{2}$$

$$\partial F / \partial t + u \cdot \nabla F = 0 \tag{3}$$

In the above equations, the variables u, p, ϑ, g, f_{st}, ρ, and F represent the velocity vector, pressure, kinematic viscosity, gravitational acceleration, surface tension force per unit volume, water density, and fluid fraction, respectively. The scalar function F is used to represent cells containing fluid: F equals one for completely filled cells, zero for empty cells, and a value between zero and one for partially filled cells (Khoshkonesh et al., 2019).

Turbulence simulation method

In this study, the Large Eddy Simulation (LES) turbulence method was employed to address large-scale structures within the grid, while sub-grid scale (SGS) stresses were used to capture minor scale dynamics. This approach proves highly effective in investigating time-dependent, three-dimensional properties of turbulent flows, offering a more detailed representation of turbulent flow characteristics compared to two-equation models (Khoshkonesh et al., 2023).

The interaction of small eddies within the flow field is modeled using a length scale, L_t, which is smaller than the length of the vortices responsible for carrying the kinetic energy. The computation of SGS stresses is accomplished using the following Eqs. (4–6):

$$L_t = (\delta x \, \delta y \, \delta z)^{1/3} \tag{4}$$

$$\tau_{ij} - \delta_{ij}\tau_{ij}/3 = -2S_{ij}\vartheta_t = -2(2S_{ij}S_{ij})^{0.5} \, S_{ij} \, (C_s L_t)^2 \tag{5}$$

$$S_{ij} = (\partial u_i / \partial x_j + \partial u_j / \partial x_i)/2 \tag{6}$$

Here, τ_{ij}, S_{ij}, ϑ_t and C_s represent the stress and strain rate tensors, turbulent viscosity, and Smagorinsky's coefficient (Smagorinsky, 1963), which is set to 0.167 as per Kim et al. (2017).

Air entrainment model

The involved air entrainment model, as proposed by Hirt (2003), assumes that surface aeration takes place when a destabilizing force, which is linearly correlated with the kinetic energy of turbulence, surpasses a stabilizing force primarily influenced by gravity and surface tension. Subsequently, this process introduces a specific volume of air into the water, as detailed in Eqs. (7–9).

$$L_t = (CNU^{0.75}k_t^{1.5})/\varepsilon_t \tag{7}$$

$$P_t = \rho k_t; \text{ and } P_d = \rho g_n L_t + \sigma/L_t \tag{8}$$

$$\delta V = \begin{cases} K_a K_s [2(P_t - P_d)/\rho] & \text{if } P_t > P_d \\ 0 & \text{if } P_t < P_d \end{cases} \tag{9}$$

where, CNU, k_t, ε_t, g_n, σ, δV, K_a, and K_s correspond to the constants (CNU being 0.09), turbulence kinetic energy, turbulence dissipation, the gravitational component perpendicular to the free surface, the coefficient of surface tension, volume of entrained air per unit time, coefficient of proportionality, and surface area, respectively. This model facilitates a thorough comprehension of the entrainment process. Post-entrainment, the air dynamics are delineated through successive density evaluation and drift-flux models (Dong et al., 2019).

Sediment transport models

The present study incorporates steady sediment transport models including both bedload and suspended load to represent sediment balance in the model, enabling a detailed visualization of bed scouring (Okhravi et al., 2022, 2023). To accurately quantify changes in substrate topography resulting from these sediment transport processes, the equations of Meyer-Peter and Muller (1948), Nielsen (1984), Van Rijn (1984), and Soulsby-Whitehouse (1997) were evaluated. This comprehensive approach allows us to consider the complex interactions and influences of these processes on substrate profile modifications. The equations consider the physical properties of water and sediment, as well as the critical Shields parameters, which play a significant role in the sediment entrainment process.

There is a consensus that the flow turbulence in dam break wavefront differs significantly from steady boundary layer flow (Catucci et al., 2021; Khoshkonesh et al., 2023). In cases where the flow dynamics and sediment transport vary rapidly over time, transient or unsteady flow models may be more suitable for accurate predictions (Dodangeh and Afzalimehr, 2022). However, the present study primarily focuses on investigating the effects of bed level differences on the wavefront and downstream erodible beds.

In dam break scenarios, it is considered that the flow dynamics may stabilize relatively quickly after the initial surge, leading to a quasi-steady state. Furthermore, the study employs the non-equilibrium sediment flux in modelling scour, which is fully coupled with the hydrodynamic model (An et al., 2015). This allows the simulation of bed level updates for each time step, which are relatively short in this study. By using this approach, the research aims to capture the transient sediment transport dynamics adequately. Nevertheless, it is essential to acknowledge that the quasi-steady state assumption has limitations, and the dynamics of sediment transport in dam break waves can be complex.

Convergence and stability criteria

The central difference method was employed for all momentum components, excluding advection. Second-order accuracy approximation were employed for both time and spatial dimensions when dealing with the acceleration and viscosity terms. To ensure stability and convergence, the time step (δt = 0.1 s) was chosen, based on the Courant-Friedrichs-Lewy (CFL) criteria. This CFL condition links the time step to the spatial interval, a principle outlined by Parambath (2010).

The convergence criteria demanded that the iteration residuals remain below 0.001. The weighting factor was set to zero for second-order approximations, indicating that fluid motion and diffusion were constrained to a single grid cell. To ensure stability, it was imperative to minimize weighting factors, a practice adopted to prevent excessive solution smoothing, as emphasized by Hirt and Nichols (1981) and Yao (2004).

Initial and boundary conditions

The computational domain was discretized into three mesh blocks using a structured mesh approach. Block 1 represented the water fraction of the upstream channel (half-section) at the dam site, while Block 2 encompassed the other upstream half-section on the dam site. Block 3 covered the downstream part of the channel (see Fig. 1 for illustration). Boundary conditions included a free surface with zero shear stresses and a 'no-slip' condition applied to the channel bottom and side walls. Upstream reservoir flow velocities were set to zero to ensure smooth transitions between mesh blocks.

The initial conditions were determined based on the water reservoir depth (D_w), upstream substrate depth (D_{us}), and downstream substrate depth (D_{ds}). The dimensions of the computational domain were scaled to match the geometrical and physical conditions of the flume model studied by Leal et al. (2003). Additionally, the mesh resolution was refined near fixed boundaries and interfaces in a nonconforming manner to enhance accuracy in critical areas. By employing this approach, the study aimed to ensure an appropriate representation of the flow dynamics and sediment transport processes, especially in regions near boundaries and interfaces, which are crucial for accurate simulations.

RESULTS AND DISCUSSION
Model verification

The model was validated using experimental data from dam break over mobile bed experiments conducted by Leal et al. (2003) and Spinewine and Capart (2013) (hereafter referred to as Ls and Sp, respectively). The necessary information, including model geometry, hydraulic and sediment bed conditions, and numerical setup characteristics, can be found in Tables 1, 2, and 3. The comparative analysis of free surface evolution and bed deformation was conducted based on experimental data from Spinewine and Capart (2013) and Leal et al. (2003). Fig. 2 presents the comparison of observed and simulated results, enabling a critical assessment of the numerical model's predictive accuracy in capturing complex fluid-sediment interactions. Fig. 2 illustrates a good level of agreement between experimental and numerical results. However, some cases reveal a minor tendency for overestimation in both the wavefront distance and free surface height. Potential explanations for these observed discrepancies may be attributed to (a) inconsistencies in the experimental setup or measurement errors, (b) inherent simplifications and assumptions in modelling the complex dynamics of wave-sediment interactions during dam break over mobile beds, and (c) uncertainties in the parameters of the sediment transport formulation.
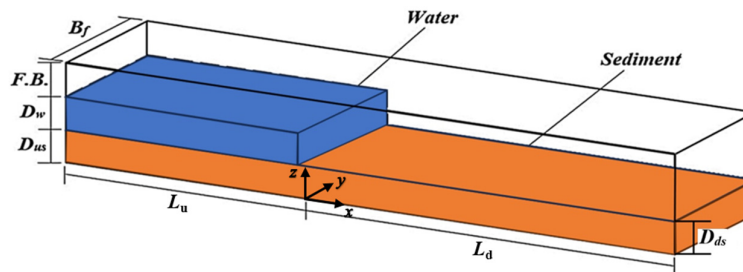

Fig. 1. Setup configuration of the dam break over an erodible bed.

Table 1. Experimental characteristics of dam break reference experiments.

Study	Flume dimensions $x \times y \times z$	Initial water depth	Tailwater depth	Sediment depth in the downstream channel	Reservoir's water volume	Verification parameters
	V (m³)	D_0 (m)	D_t (m)	D_{s0} (m)	V_w (m³)	
Spinewine and Capart (2013)	6×0.25×0.7	0.35	0	0.15	0.27	free surface level (D_w) and bed (D_s) profiles
Leal et al. (2003)	19.2×0.5×0.7	0.4	0	0.071	1.93	

Table 2. Characteristics of sediment bed in dam break reference experiments.

Models	Mean diameter d_{50} (mm)	Specific density S_g	Fall velocity w (cm/s)	mobility w^*	Entrainment coefficient
Sp	1.82	2.683	0.18	1.32	0.018
Ls	0.77	2.65	0.092	0.89	0.018

There are notable differences in sediment characteristics between the studies conducted by Spinewine and Capart (2013) and Leal et al. (2003). Spinewine and Capart (2013) focused on a dam break scenario featuring a downstream channel with a sediment depth of 0.15 m, whereas Leal et al. (2003) observed a thinner sediment depth of 0.071 m. Furthermore, the sediment analysed in the Spinewine and Capart (2013) study exhibited a larger mean diameter, d_{50}, of 1.82 mm, which is nearly double the 0.77 mm diameter reported by Leal et al. (2003). Notably, the sediment fall velocity differed between the two studies. The first study recorded a sediment fall velocity of 0.18 cm/s, which is approximately twice the value of 0.092 cm/s observed in the second study (Table 2). Intriguingly, despite these disparities, both studies shared an identical entrainment coefficient of 0.018. However, Spinewine and Capart (2013) reported a higher mobility w^*, of 1.32, in contrast to the value of 0.89 noted by Leal et al. (2003).

The computational results and sensitivity analysis related to mesh resolution, turbulence models, and bed load transport formula under different scenarios detailed in Fig. 2 have been presented in Table 3. The performance of the models and the analysis of the results were evaluated using the normal root-mean-square error (NRMSE) metric (Eq. 10) as proposed by Yang et al. (2018):

$$\text{NRMSE} = \sqrt{\sum_{i=1}^{n} (Y_{i,e} - Y_{i,c})^2} \Big/ \left(Y_{i,e\,(max)} - Y_{i,e\,(min)}\right) \qquad (10)$$

Here, $Y_{i,e}$, $Y_{i,c}$, $Y_{i,e\,(max)}$, and $Y_{i,e\,(min)}$ represent the experimental (i,e)

and computational (i, c) values of the corresponding parameter Y. NRMSE values between zero and 0.1, 0.1 and 0.2, 0.2 and 0.4 indicate high, suitable, and average model accuracy, respectively. The evaluation of model performance was based on errors NRMSE_{Dw} and NRMSE_{Ds}, which represent the predicted water surface height (D_w) and substrate depth (D_s), respectively. The model demonstrated high accuracy in predicting D_w and average accuracy in predicting D_s. Notably, the LES method combined with the Van Rijn (1984) bed load transport formula showed the highest accuracy in models Sp_2, Sp_5, Ls_1, and Ls_3 (Table 3, cases b, e, i, and k in Fig. 2), leading to subsequent models being conducted using this combination.

The computational times (T_p) for both the Sp and Ls cases have been documented in Table 3. The associated experimental dam break times were 1.25 s for Sp and 4 s for Ls, respectively, with a fixed time step of 0.1 s. The automatic selection of this time step was based on considerations of convergence, stability criteria, and the need to accurately capture subsequent events during the evolution of the dam break wave. It was observed that the turbulence models and bed load formula had negligible effects on T_p, while the primary controlling variable for simulation time was the mesh resolution.

In conclusion, this study highlights the accuracy and applicability of the turbulence models and bed load formula in predicting dam break wave dynamics over mobile beds. The mesh resolution was identified as the key factor affecting computational time, emphasizing the importance of optimizing mesh refinement for efficient simulations.
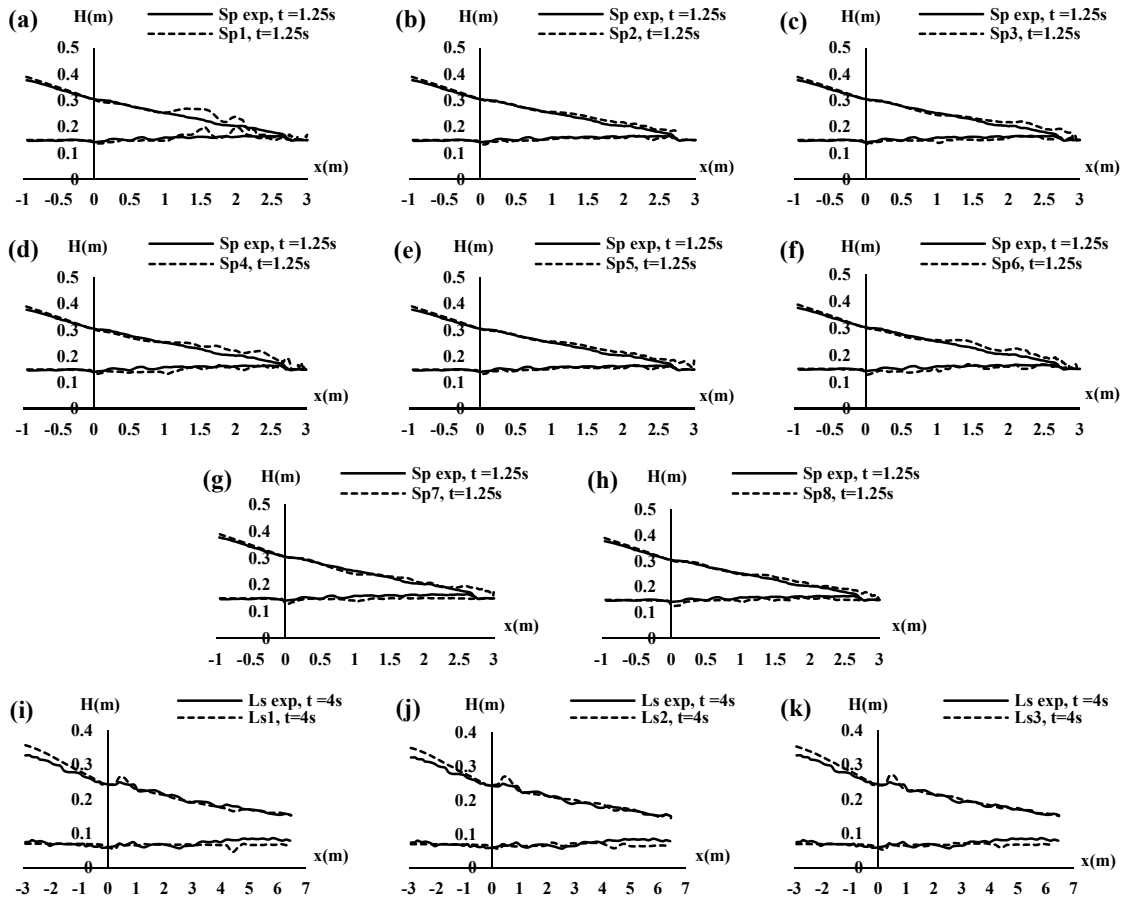
Fig. 2. Comparative analysis of free surface and substrate profiles in the present numerical study with experimental results from Spinewine and Capart (2013) at t = 1.25 s (cases a to h) and Leal et al. (2003) at t = 4 s (cases i to k) as detailed in Table 3.

Table 3. Sensitivity analysis of the mesh resolution, turbulence closer schemes, and bed load transport formulas.

Models	Bed load transport formula	Turbulence model	Number of cells	T_p (h)	NRMSED_w	NRMSED_s
a-Sp$_1$	Van Rijn	LES	1874642	2.13	0.076	0.463
b-Sp$_2$	Van Rijn	LES	963590	0.87	0.042	0.205
c-Sp$_3$	Van Rijn	LES	499302	0.41	0.052	0.314
d-Sp$_4$	Van Rijn	k-e	963590	0.93	0.066	0.400
e-Sp$_5$	Van Rijn	k-w	963590	0.86	0.046	0.216
f-Sp$_6$	Van Rijn	RNG	963590	0.94	0.058	0.363
g-Sp$_7$	Mayer-Peter and Muller	LES	963590	0.83	0.044	0.423
h-Sp$_8$	Nielsen	LES	963590	0.81	0.039	0.361
i-Ls$_1$	Van Rijn	LES	2211956	5.37	0.089	0.250
j-Ls$_2$	Van Rijn	LES	1670724	2.75	0.090	0.281
k-Ls$_3$	Van Rijn	LES	1204458	2.94	0.086	0.261

Substrate level difference and bed material

In this study, we investigated the interaction between the sediment bed and the dam break wave while considering the influence of substrate level difference and bed material. To quantify the difference in substrate depth between the downstream and upstream channels, we introduced the variable $d = D_{ds}/D_{us}$ as the ratio of D_{ds} (initial substrate depth at downstream channel) to D_{us} (upstream channel elevation) (refer to Figs. 1 and 3). A value of "d" was defined as $d = 1$ to represent no substrate level difference.

The present study presents the results of 10 numerical simulations with different d values ranging from 0 to 1, where 0 represents the highest-level difference (see Table 4). Based on the cases reported in Table 4, using sand-bed material, we observed that an increase in the value of d led to a decrease in T_p, indicating a reduction in computational runtime. The results showed the value of $d = 0.25$ was associated with the longest runtime. Conversely, higher d values resulted in a decrease in the number of iterations N_{mi} and, consequently, a decrease in the processing simulation time. Hence, the simulations with the smallest d value incurred the highest computational costs.

Evolution of free surface and mobile bed profiles

The dam break wave evolution was analysed in three stages ($t = 1$, 3, and 5 s), representing the initial, middle, and final stages of the phenomenon. The analysis focused particularly on the near field, which refers to the region immediately surrounding the dam, where significant changes in flow characteristics occur (Aleixo et al., 2010). One key characteristic of the near field regime is the presence of a strong non-horizontal component in the velocity field. This indicates that the flow velocities in this region are not predominantly parallel to the water surface but exhibit substantial vertical and lateral components.

The progression of the dam break flow for different simulation cases was depicted in Fig. 3, highlighting the variations in downstream bed erosion based on various bed level configurations (Table 4). Notably, significant erosion and deposition occurred in the near-field or under the wavefront region. Fig. 3 illustrated how increasing d values attenuated the impacts of the dam break. In Sp$_1$ and Ls$_1$ (corresponding to the highest bed level differences), the maximum flow velocity was more than 2.5 times the surface wave velocity ($C_w = (gD_w)^{0.5}$), with the maximum wavefront velocity approximately 1.25 times the measured velocity by Ritter (1892) ($u_{max} = 2C_w$) according to Nielsen (2018).

At the initial stage ($t = 1$ s), the substrate material and level difference did not significantly affect the dam break flow velocity within the reservoir. Generally, as d values increased, the curvature of the free surface and substrate profiles in the near field decreased, leading to a reduction in the maximum flow velocity and the thickness of the sediment sheet-flow layer downstream of the scour formation. Additionally, the water height D_w (see Fig. 1) also plays a crucial role in determining flood wave propagation velocity. Specifically, lower water depths result in slower flood wave propagation downstream, as reported by Vosoughi et al. (2020).

The downstream channel's free surface fluctuations decreased as *mobility factor w** (Table 2) decreased and d values increased from zero to one. Notably, distinct scour holes were observed in the near field for cases Sp$_2$ to Sp$_4$ and Ls$_2$ to Ls$_4$. The most significant flow disturbance and substrate deformation in the downstream channel occurred at $d = 0.25$ in cases Sp$_2$ and Ls$_2$, leading to the formation of anti-dunes in the near field. Comparing Sp$_2$ and Ls$_2$, the height of the anti-dune in Sp$_2$ was slightly higher, possibly attributed to the lower *w** and smaller particle mean diameter (*w** $= 0.89$ and $d_{50} = 0.77$ mm) in Ls$_2$ than in Sp$_2$ (*w** $= 1.32$ and $d_{50} = 1.82$ mm). Moreover, an increase in d values correlated with a decrease in the wavefront advancing distance.

Profiles of transverse and vertical Velocities

The transverse and vertical velocities during dam failure over a moving bed are crucial as they dictate flow dynamics, scouring, and depositional patterns, all of which are vital for predicting structural stability and managing environmental impacts.

Upon analysing the results, it was evident that the transverse velocity v varied between –0.75 m/s and 0.7 m/s for Sp cases (Fig. 4). The velocity fluctuations for Ls cases were notably lower compared to Sp cases, except for $d = 1$ (Sp$_5$ and Ls$_5$). The transverse velocity exhibited fluctuations across the flume width (refer to Fig. 1), with an approximate symmetry near the sidewalls. The vertical downward velocity w (negative values) decreased in the z-direction with increasing d and was slightly higher for Ls cases compared to Sp cases. For Sp cases, the vertical velocity ranged from $−1.8$ m/s to 0.3 m/s, while for Ls cases, it ranged from $−1.8$ m/s to 0.1 m/s.

Throughout the near field, the transverse and vertical velocities changed by approximately 1 m/s and 2 m/s, respectively, from the initial to the final stages. Hence, the vertical velocity was roughly twice the transverse velocity in the near field. The curves of vertical velocity exhibited the highest
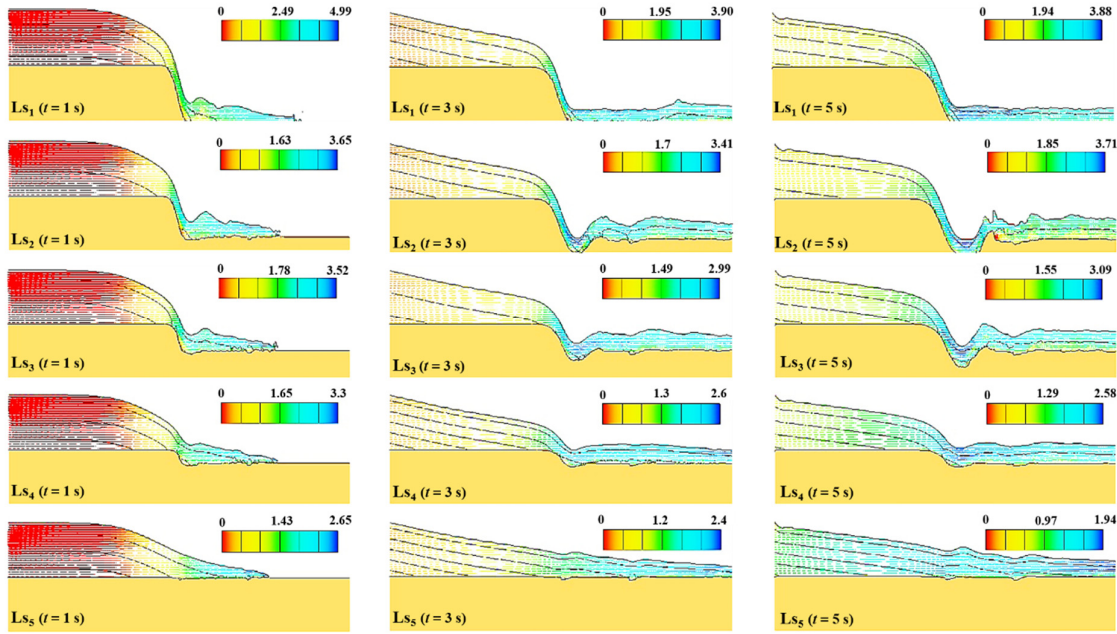
Fig. 3. Free surface and substrate profiles in all Sp and Ls cases at $t = 1$ s, $t = 3$ s, and $t = 5$ s, arranged left to right (note: the colour contours correspond to the horizontal component of the flow velocity (u), expressed in m/s).

**Table 4.** The simulations properties of the studied cases.

Cases	Run's name	Level difference ratio	Dimensions (m) (refer to Fig. 1)	Run time	Processing time for each thread × 10³	Processing time for each iteration of N_{mi}
		$d = D_{ds}/D_{us}$	$D_{us}, D_{ds}, F.B, B_f, L_u, L_d$	T_p (h)	T_d (s)	T_i (s)
1	Sp₁	0	0.4, 0, 0.02, 0.5, 5, 5	3.44	1.548	1.856
2	Sp₂	0.25	0.4, 0.1, 0.02, 0.5, 5, 5	4.77	2.147	2.288
3	Sp₃	0.5	0.4, 0.2, 0.02, 0.5, 5, 5	4.73	2.129	2.571
4	Sp₄	0.75	0.4, 0.3, 0.02, 0.5, 5, 5	3.59	1.616	2.530
5	Sp₅	1	0.4, 0.4, 0.02, 0.5, 5, 5	2.57	1.156	2.2
6	Ls₁	0	0.4, 0, 0.02, 0.5, 5, 5	2.62	1.179	1.788
7	Ls₂	0.25	0.4, 0.1, 0.02, 0.5, 5, 5	4.97	2.236	2.381
8	Ls₃	0.5	0.4, 0.2, 0.02, 0.5, 5, 5	4.24	1.908	2.249
9	Ls₄	0.75	0.4, 0.3, 0.02, 0.5, 5, 5	3.34	1.503	2.249
10	Ls₅	1	0.4, 0.4, 0.02, 0.5, 5, 5	2.76	1.242	2.202

and first inflection point, signifying a sharp change in velocity trend, near the free surface. This position shifted to the right side of the w-axis from the first to the last stages but remained relatively stable for Ls₄ and Ls₅. For Sp₅ at the initial stage, the sign of the vertical velocity changed from positive to negative with increasing z-values, possibly due to backwater caused by the dam break's impact on the downstream substrate ($d = 1$) at the initial stage. However, the positive vertical velocity value was negligible for Sp₅ and Ls₅.

Flow regime dynamics in dam break

The Froude number Fr serves as a descriptor for the variations in flow regime during dam failures based on depth-averaged velocity. In the current study, Fr showed relatively little change in the middle to last stages (refer to Fig. 5). Nevertheless, the trans-critical flow was observed in all cases as the flow regime

transitioned from subcritical ($Fr < 1$) to supercritical ($Fr > 1$) in the near field. This transition occurred from the upstream near field ($x \approx -1$ m) towards the dam, with an increase in d from 0 to 1 for all cases. Additionally, Fr values decreased with increasing d values in the middle and last stages, indicating transient flow conditions in the downstream channel. It was evident that Fr was highest in the wavefront region, as there was a strong flow shear gradient dominating the substrate drag, particularly during the initial stage at the vicinity of the near field. This supercritical condition and shallow flow depth at $t = 1$ s led to significant sediment entrainment. A similar pattern of results was obtained in the study conducted by Gu et al. (2023) on silted-up dam break flow, particularly during the initial stage at approximately 0.9 s, where rapid washed-out sediments were observed. Their observations indicated that the front velocity of the dam break flow decreased with an increase in the height of the silted-up sediment.
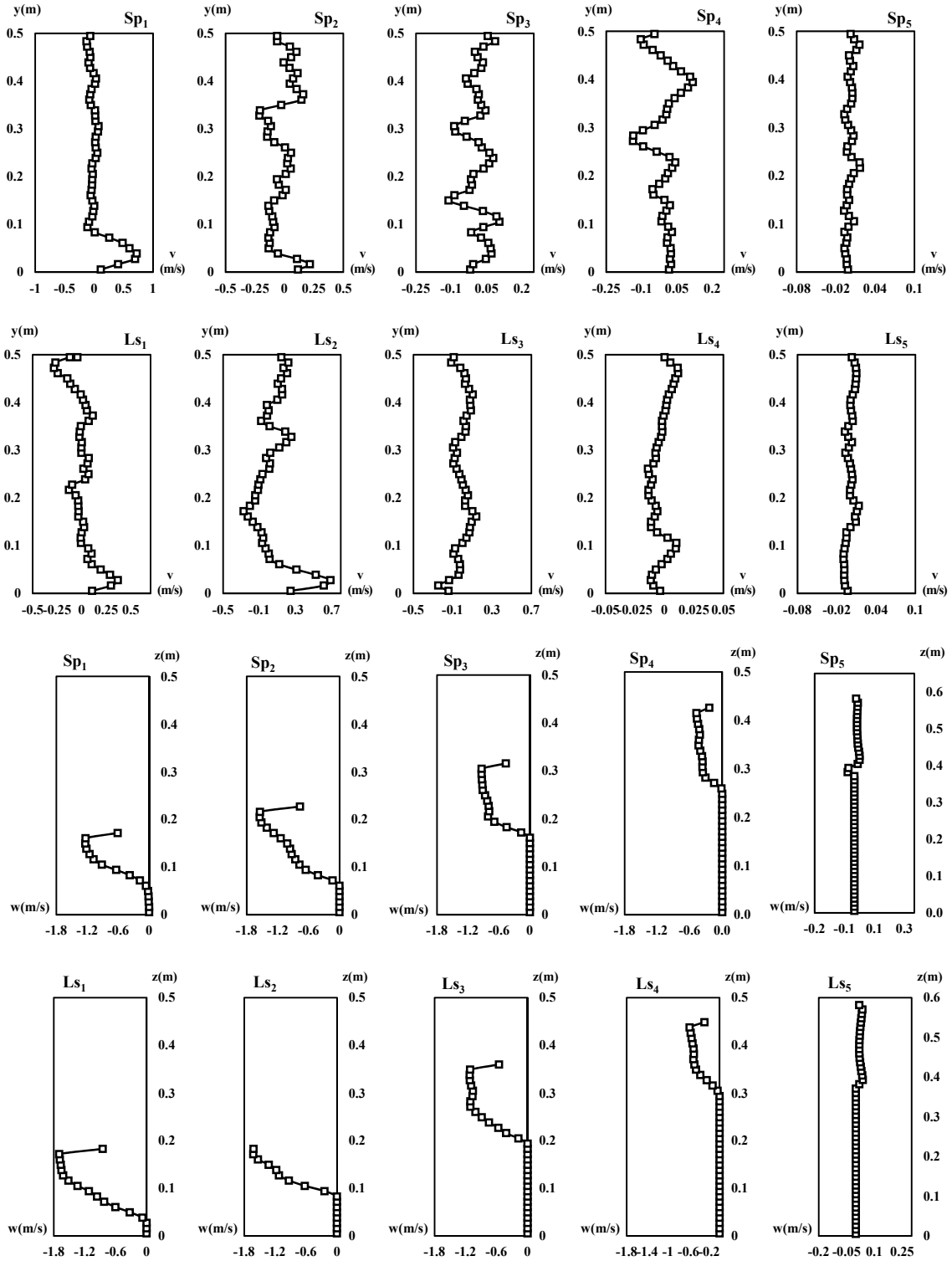
Fig. 4. Transverse (v) and vertical (w) velocities near the dam ($x = 0.03$ m) at $t = 3$ s for all simulations reported in Table 4

Throughout the middle to last stages, Fr values were consistently higher in Ls cases (case numbers 6–10 in Table 4) compared to Sp cases (case numbers 1–5 in Table 4) in the downstream channel. This suggests that finer sand particles in Ls cases with less mobility (w^* in Table 2) offered less resistance against the flow evolution during the dam break stages. As a result, Fr values remained nearly identical within the reservoir for all cases due to the gradually varied flow within the reservoir from the initial to middle stages. In all cases, critical flow conditions were observed in the near field ($x \approx 0$ m).

To delineate substrate roughness conditions, the parameter of particle Reynolds number ($Re_* = u_* k_s / \vartheta$) was utilized (Gualtieri
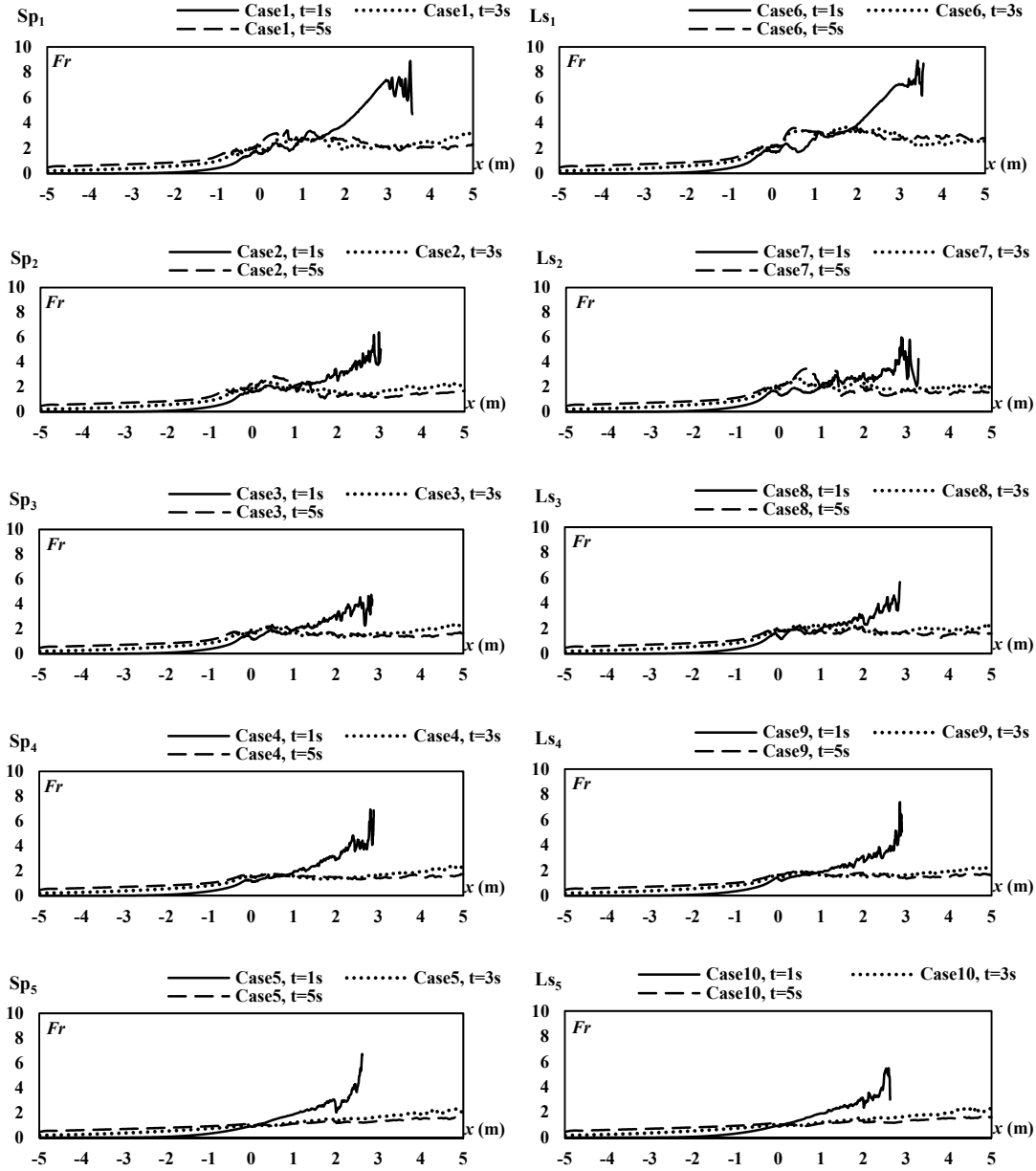
Fig. 5. Spatial variation of Froude number (*Fr*) along the central flume axis for all cases at different simulation stages (*t* = 1 s, *t* = 3 s, and *t* = 5 s).
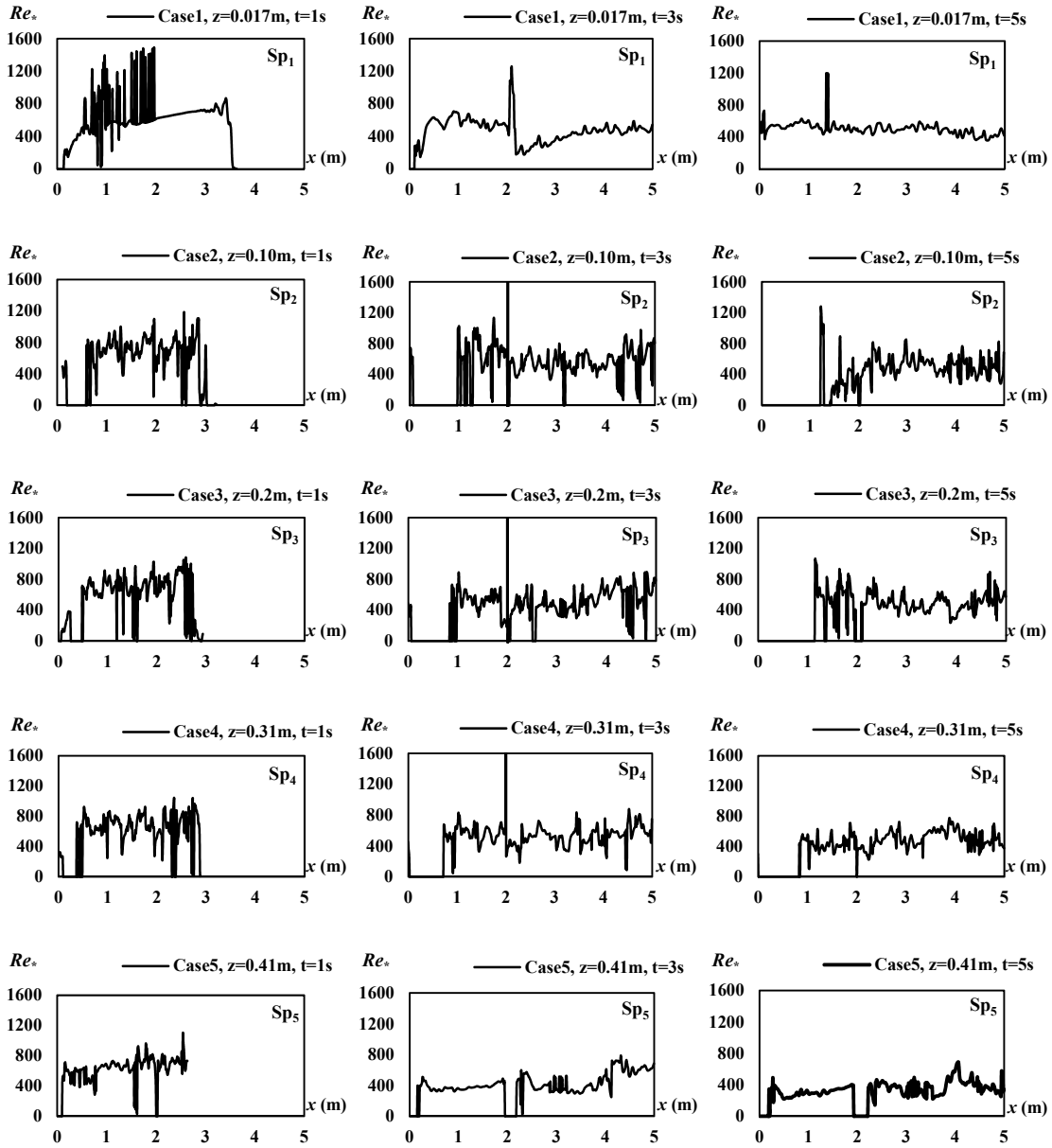
et al., 2018). In this equation, u_* and k_s ($k_s = d_{50}$) represent the shear velocity in the vicinity of the substrate and particle roughness, respectively. The shear velocity u_* is evaluated at $z = D_{us}$ and D_{ds}, respectively, within the reservoir and the downstream channel. It is important to note that the substrate particles were considered spherical in all modelling.

Based on the values of Re_* and the flow classification of van Rijn (1984), three substrate conditions were identified: $Re_* > 200$ represents rough turbulent flow conditions, $3 < Re_* < 200$ represents transient conditions, and $Re_* < 3$ represents smooth substrate conditions. As shown in Fig. 6, at the initial stage of all simulations (e.g. all Sp_s in Fig. 6), Re_* increases from zero to over 660 at the upstream side of the channel, until reaching the dam's location. Then, it changes from about 180 to over 590 at the middle stage and from approximately 320 to over 600 at the

last stage. Notably, for Sp_5, with a higher *d* value, Re_* is lower compared other simulations.

It is worth noting that Re_* is roughly reduced with increasing *d* values, particularly across the downstream channel. Additionally, Re_* values decreased due to flow release from the outlet, leading to a reduction in velocity at the middle and last stages. However, the turbulent-rough condition prevailed throughout the flume, except in the near field during the middle stage. This could be attributed to the formation of the scour hole in the near field, which caused (i) an increase in flow depth over the scour hole, (ii) head loss due to flow disturbance and backwater, and (iii) the formation of hydraulic jumps downstream of the scour hole.

At *t* = 3 s, the reservoir shows faster water depletion compared to *t* = 1 s, resulting in the dominance of the rough and transient

Alireza Khoshkonesh, Blaise Nsom, Saeid Okhravi, Fariba Ahmadi Dehrashid, Payam Heidarian, Silvia DiFrancesco

Fig. 6. Particle Reynolds number (Re_*) values along the flume central axis for all SPs at different simulation stages, arranged left to right ($t = 1$ s, $t = 3$ s, and $t = 5$ s).

particle's relative velocity with respect to the surrounding fluid at the beginning point of the reservoir's depletion. Subsequently, during the last stage at $t = 5$ s, the reservoir is almost completely discharged, leading to a reduction in flow velocity and free surface height within the reservoir. The numerical results of silted-up dam break flow over a dry bed, as reported in the study by Meng et al. (2022), exhibit a similar pattern of computed velocity profiles along the longitudinal direction over time. Notably, the lowest velocity was observed during the middle stage of the dam break flow. As a result, the reservoir substrate roughness changes from turbulent and rough to transient conditions at $t = 5$ s. In the near field, during the initial to last stages, the substrate roughness changes from smooth to rough, turbulent conditions within the distance $x \approx 0$–2 m. This distance becomes more extended in the near field as the stages progress from the initial to the last.

Air entrainment

In this study, we approach the dam break problem as an incompressible one-fluid flow, considering air entrainment as an additional model to consider turbulence processes. In Fig. 7, the air entrainment region is observed to be significantly deformed during the very initial stages ($t = 0.1$–0.25 s). At $t = 0.1$ s and 0.15 s, it appears bowl-shaped in the bottom region of the wavefront. Subsequently, it develops into a tongue-shaped formation under the wavefront in the downstream channel. The entrapped air velocity vectors demonstrate the evolution of rotational air-water flow. The wavefront tip region moves upward as air entrapment increases through the wavefront at $t = 0.2$ s and 0.25 s. From Figs. 8 and 9, it is evident that the greatest mixing of air and water (indicated by dark colour) occurs along the water-sediment interface in the wavefront region. Notably,
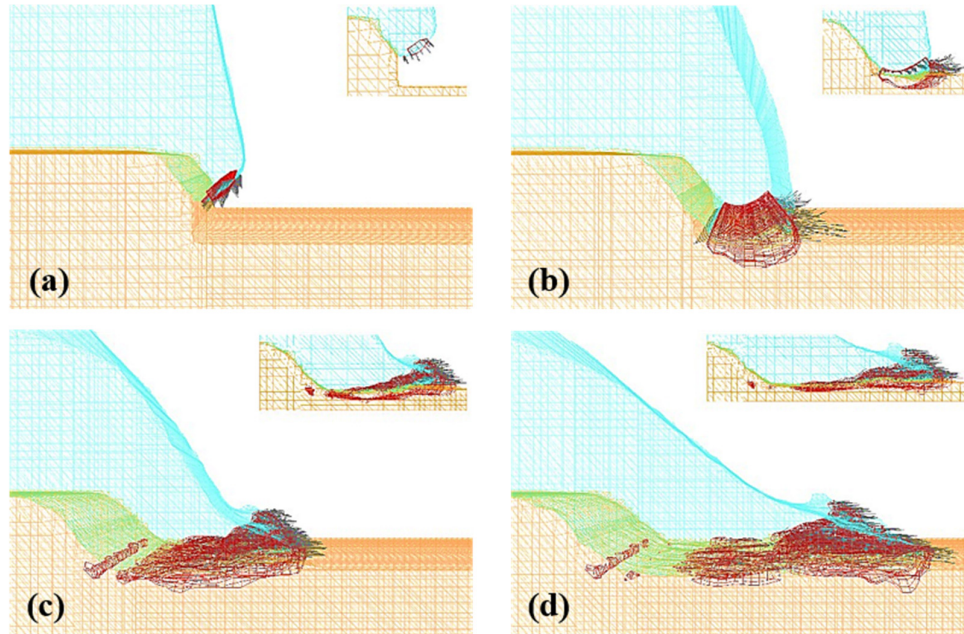
88

Fig. 7. Air entrapment in the wavefront region of case Ls$_4$ at various time intervals. Snapshots captured at specific time points: a) 0.1 s, b) 0.15 s, c) 0.2 s, and d) 0.25 s.
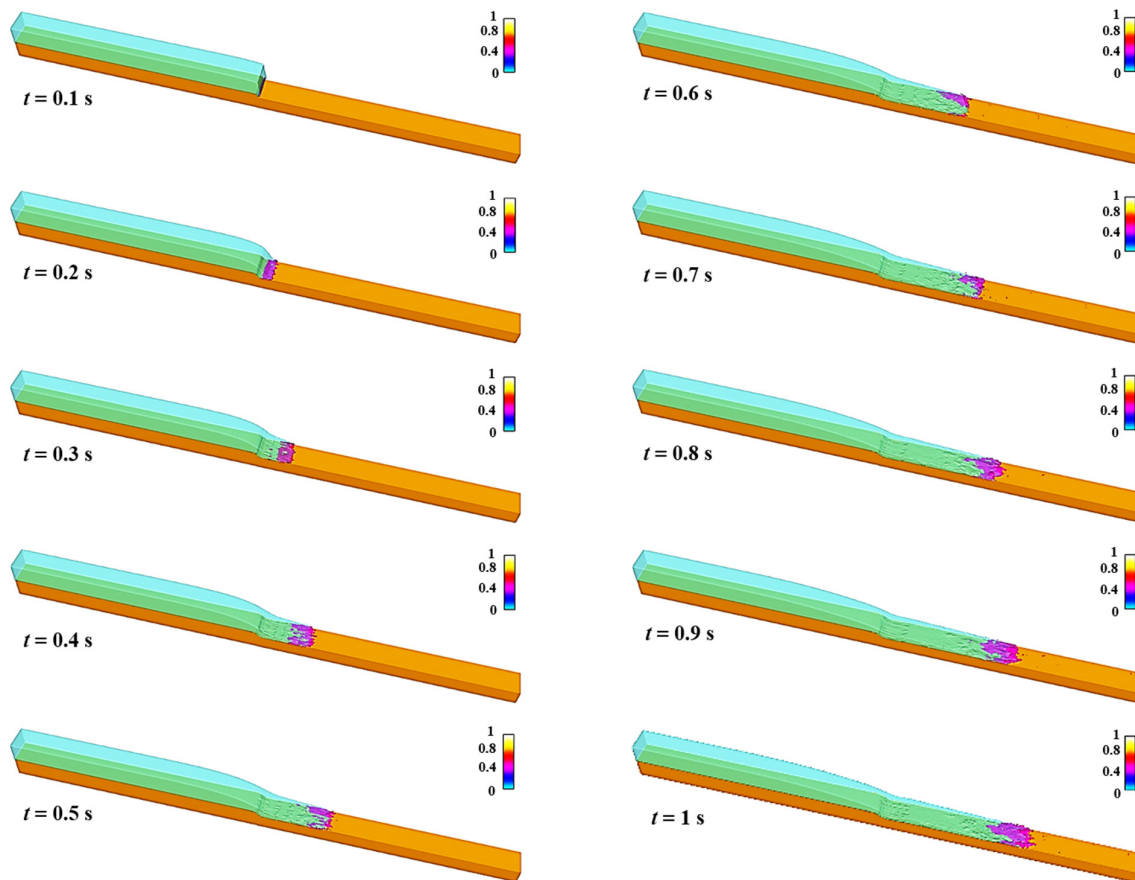

Fig. 8. Iso-surface of F_{air} in case of Ls$_4$ at $t = 0.1$ s to 1s.

the entrapped air values are significantly increased in the wavefront, reaching the maximum value $F_{air} = 1$ at $x = 3$ m (Fig. 9). Similarly, Bahmanpouri et al. (2021) reported numerical results showing that the maximum void fraction was associated with the maximum flow velocity in the wave-front zone. However, in other flow regions, there is no considerable air entrapment. On the other hand, Desombre et al. (2013) observed that air bubbles were trapped in the swash front and released from its rear. In our study, we found that air entrapment begins from the bottom of the wavefront and then develops under the wavefront during the initial stages, continuing until the flow is discharged from the flume outlet. Additionally, the considerable rotational flow velocity results in an increase in partial dynamic pressure in the wavefront region during $t = 0–1$ s. This dynamic pressure is a result of the dominant downward motion of the dam break flow in the near field during the initial stage (Leal et al., 2003; Leal et al., 2006). The expansion and contraction of air pockets further contribute to pressure fluctuations.

Air entrapment occurs only in the near field during the very initial stages of the flow ($t = 0.1–0.25$ s). Subsequently, the water-sediment-air mixture is transported towards the flume outlet due to the evolution of the wavefront. However, partial development of the mixture upstream is also observed during the wavefront evolution. The interaction of water and air, along with rising bubbles, has a significant impact on the sediment transport processes. In this study, the drag force exerted by air bubbles is considered, which adds to the substrate resistance and causes head loss (Heller, 2011). Additionally, sediment deposition occurs predominantly in the far field, except at the outlet point, where the mixture is discharged completely through the dam break flow.

In Fig. 9, those cases Sp_1 and Ls_1 exhibit the lowest air-entrapped fraction (F_{air}) values. This can be attributed to the relatively lower resistance force of the fixed downstream region ($Hs_2 = 0$, see Fig. 1) against the wave evolution compared to the other cases. Across all cases, like Fig. 8, the highest F_{air} values

are observed in the wavefront region, specifically between 2–3 m downstream of the dam's location. However, Sp_5 and Ls_5 show lower F_{air} values compared to the other cases due to their lower downward velocity and less protruding kinetic energy (refer to Figs. 5 and 6). The distribution of air bubbles is asymmetrical with respect to the central flume axis. This asymmetry can be attributed to various factors, such as the stochastic motion of air bubbles through the wavefront, collisions between bubbles, substrate, and suspended particles, and the bursting of air bubbles at the free surface.

Sediment transport analysis

The evolution of the bed profile including erosion and sedimentation processes are accurately captured through the application of the Shields parameter. The assessment of the Shields parameter θ, based on the data provided in Table 1, is presented in Fig. 10. As depicted, there is no discernible substrate movement within the reservoir bed material during the initial stage, owing to the low flow velocity; it is noteworthy that the material on the upstream side of the channel does not reach the threshold entrainment condition. Erosion becomes significant in the reservoir substrate due to an increase in flow velocity during the final stage ($t = 5$ s). Similarly, the downstream substrate experiences erosion due to the rise in flow velocity. Likewise, the maximum ratio $(\theta/\theta_{cr})_{max}$ is observed in Sp_1 and Ls_1, both in the wavefront at $t = 1$ s and in the near field at $t = 3$ s and 5 s (where $\theta_{cr} = 0.051$, calculated using sensitivity analysis). This dominance of flow shear stresses over substrate resistance near the dam is a major factor, leading to the formation of a scour hole. Conversely, as the d value quadruples for other Sp cases, $(\theta/\theta_{cr})_{max}$ decreases to approximately one-third of the initial value. Notably, for Sp_5, the $(\theta/\theta_{cr})_{max}$ value at $t = 3$ s and 5 s shifts to the outlet, distinct from Sp_{1-4}. Furthermore, despite differences in d_{50}, ρ_s, and w^*, (i) values remain nearly equal for Sp_5 and Ls_5.
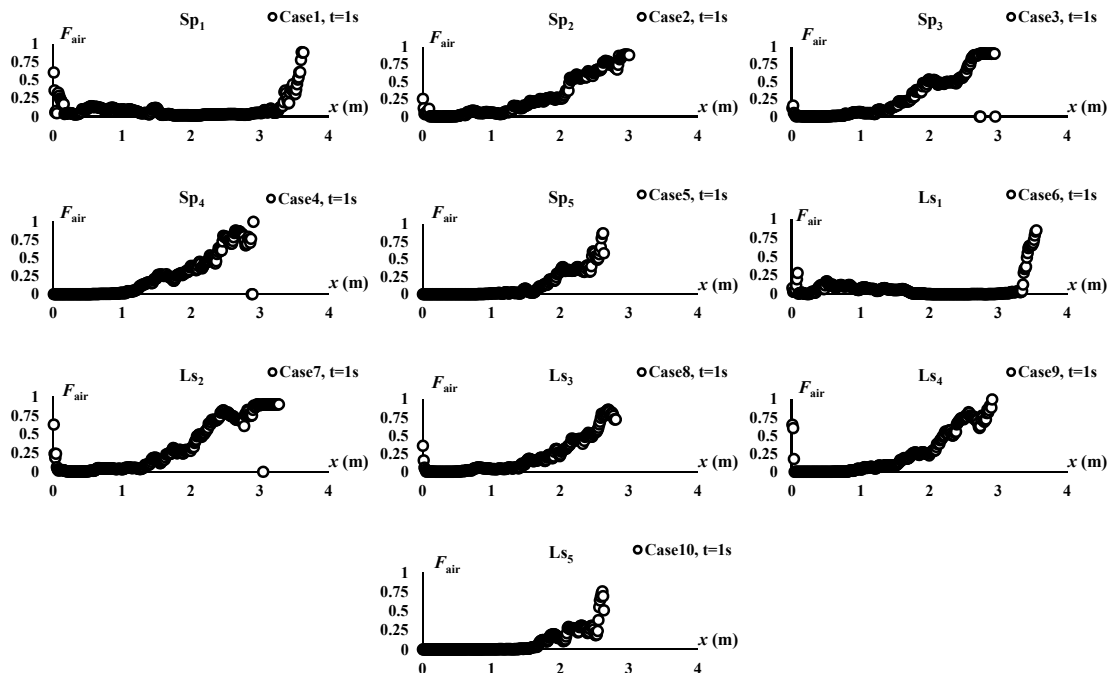

Fig. 9. Air entrainment at $t = 1$ s along the downstream channel (central flume axis).
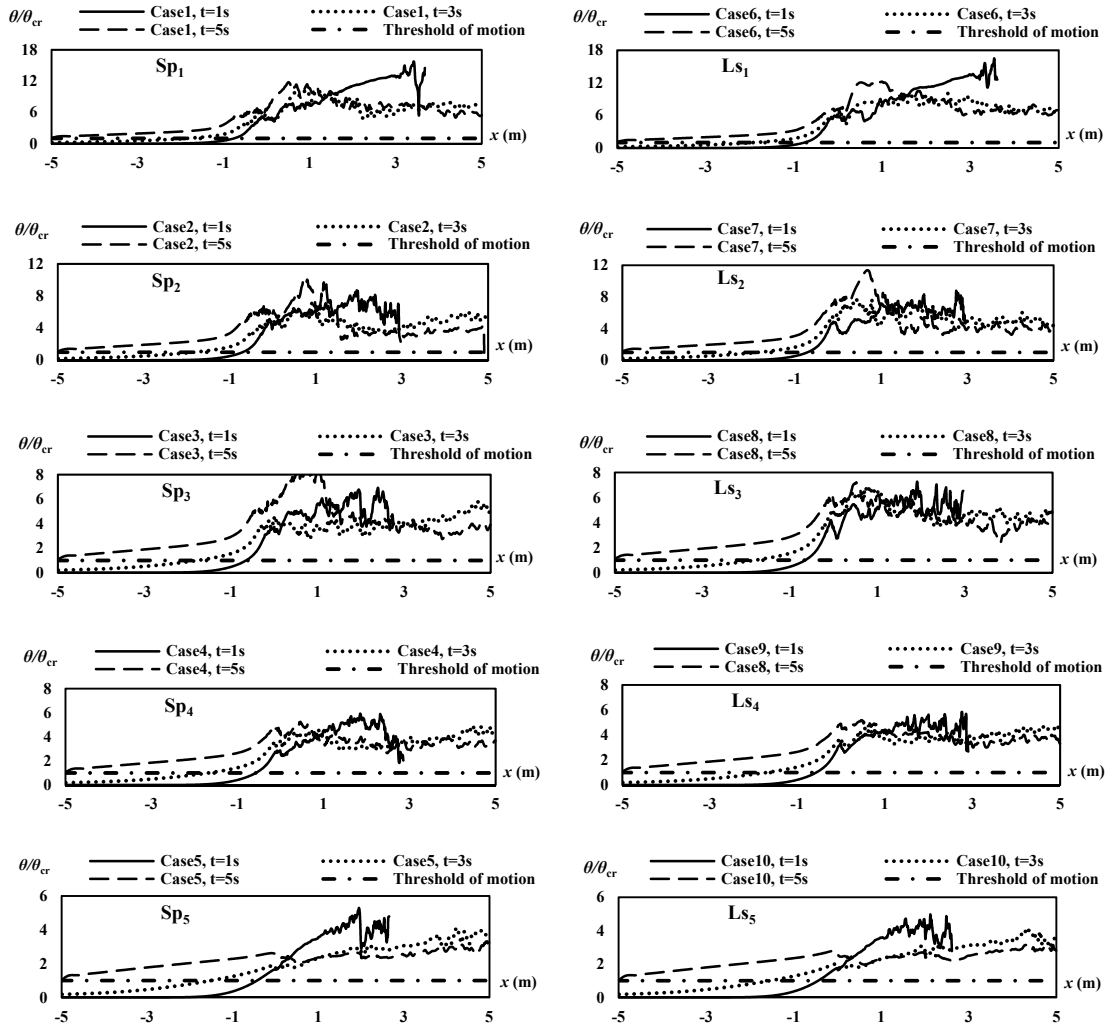
Fig. 10. Spatial distribution of Shields stress ratio (θ/θ_{cr}) along the central flume axis.

The concentration of suspended sediment, denoted as *C*, signifies the mass of sediment per unit volume of the sediment-water mixture. Fig. 11 depicts the spatiotemporal variations in concentration throughout the dam break evolution. Particularly notable are the significantly elevated values of suspended sediment concentration near the bed, especially during the initial stage. As noted by Vosoughia et al. (2020) and Gu et al. (2023), the transportation of suspended sediment not only diminishes dam break flow velocity by attenuating kinetic energy but also prolongs the time required for the formation of the dam break flow wave. Consequently, this significant concentration of suspended sediment introduces substantial resistance to the progression of the wavefront, thereby inducing rapid substrate deformation. While the findings of Fraccarollo and Capart (2002) suggest a constant sediment concentration in the near-bed regions with a minimal contribution to sediment flux transport, our current results exhibit inconsistency with this assumption during the initial stage of modelling the dam break over an erodible bed. Nevertheless, this assumption holds relatively true during the middle to last stages of the process. Notably, the downstream channel portrays a notably higher C compared to the reservoir. The detachment of particles from the substrate is intrinsically linked to flow velocity. Consequently, the concentration of suspended particles experiences an appreciable increase within the reservoir due to the intensified flow velocity during the middle and final stages. Furthermore, as observed in Fig. 11, the near-bed concentration exhibits heterogeneous and homogeneous distributions within the downstream channel and the reservoir, respectively. This phenomenon can be attributed to varying levels of flow turbulence across these regions, intense in the downstream channel and negligible in the reservoir.

In Fig. 11, the highest near-bed concentration is observed in the wavefront region, specifically between 2–3 m downstream of the dam's location for cases Sp$_{2-5}$ at $t = 1$ s. Conversely, for Sp$_1$, the greatest concentration is found in the near field region around $x \approx 0–1$ m. due to a fixed downstream bed. These findings are consistent with the works of Cao et al. (2004), Baklanov (2007), Wu and Wang (2008), Vosoughi et al. (2020), and Pintado-Patiño et al. (2021), who demonstrated that increasing sediment concentration leads to a reduction in dam break flow velocity. Hence, the insights provided by Fig. 11 complement the flow velocity analysis presented in Fig. 3 by highlighting that the peak flow velocity is concentrated at the wavefront near the dam's position. This phenomenon leads to intensified sediment deposition and elevated suspended sediment concentration downstream ($x = 2–3$ m), particularly in the initial stage. Furthermore,

91
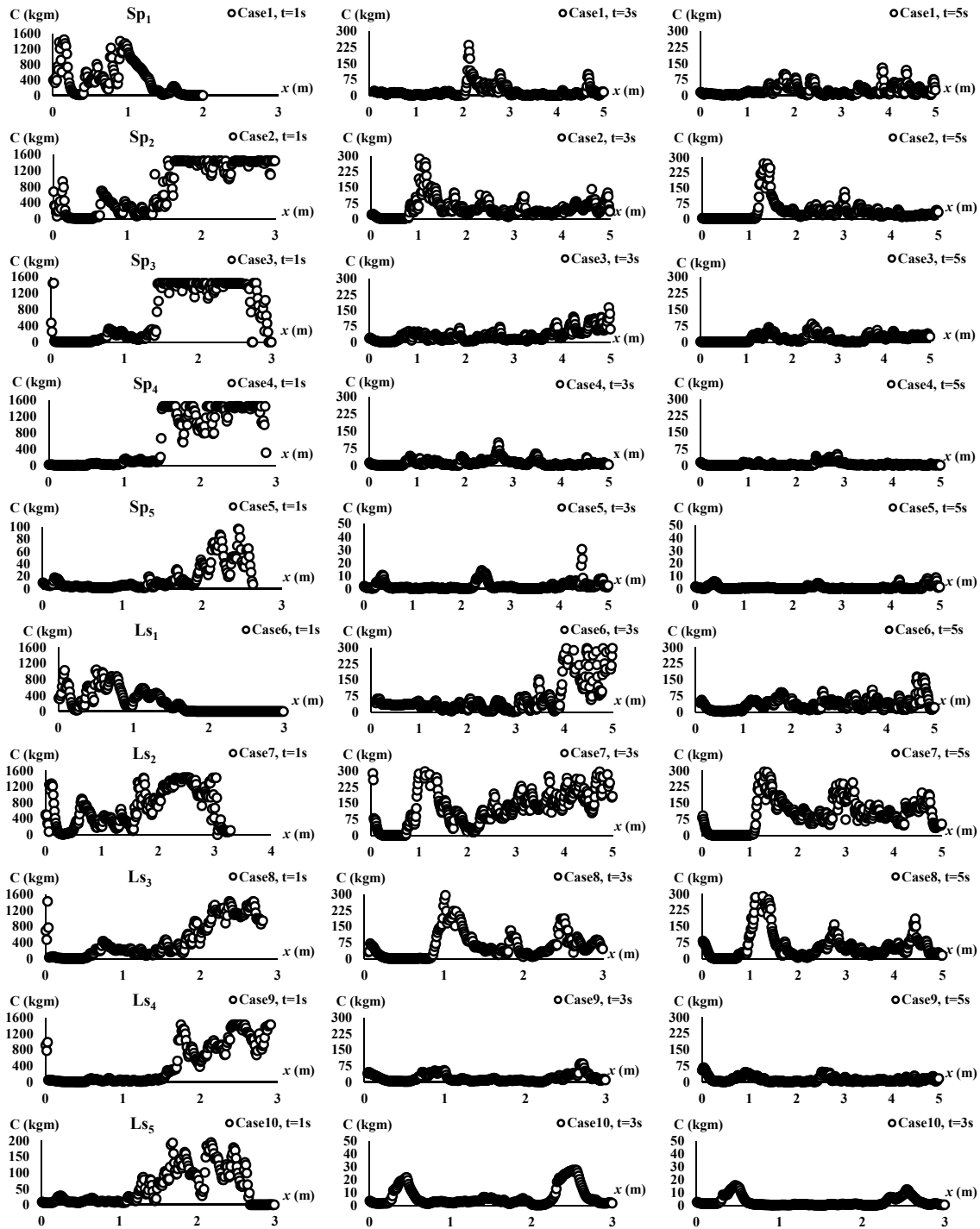
Fig. 11. Variation of near-bed concentration C (kg/m^3, abbreviated as kgm) along the downstream channel, arranged left to right ($t = 1$ s, $t = 3$ s, and $t = 5$ s).

apart from Sp$_1$, increasing the value of d results in a notable decrease in the near-bed concentration. Interestingly, Sp$_5$ exhibits considerably lower C values compared to Sp$_{1-4}$. At the initial stage, the near-bed concentration extends beyond $x > 1$ m and then experiences a dip within a small interval around $x \approx$ 2.5–3 m for Sp$_{2-5}$ and Ls$_{2-5}$. Similarly, C values decrease at $t =$ 3 s and 5 s. Additionally, across all cases, the lowest concentration values are observed during the final stage at $t = 5$

s. Among cases Sp$_{1-5}$, the concentration values for Sp$_5$ stand out as notably lower. Furthermore, for cases Sp$_{3-5}$, the near-bed concentration values are almost negligible in the near field region around $x \approx$ 0–1 m at $t = 1$ s.

In all cases except Sp$_1$ and Ls$_1$, the near-bed concentration values remain insignificant within the near field ($x \approx$ 0–1 m) during the test. This is attributed to the prevalence of bed load sediment transport mode, primarily driven by intense scouring

activities in the near field. Notably, for Ls$_1$, near-bed concentration values are lower than those of Sp$_1$ during the initial stage but become higher during the middle to last stages. Additionally, concentration values and fluctuations throughout the downstream channel are more pronounced for Ls$_1$ than for Sp$_1$ at t = 3 s and 5 s. Similarly, for Ls$_{2-3}$, concentration values are greater than those of Sp$_{2-3}$, especially during the middle and last stages, although Ls$_3$ exhibits lower C values compared to Sp$_3$ at t = 1 s. These distinctions can be attributed to variations in sediment sizes and materials. Given that the Ls experiments involve finer material (as indicated in Table 2), these particles remain suspended for longer durations and are transported farther downstream during the later stages of the simulation test. Cao et al. (2004) have highlighted that the near-bed concentration is affected by both sediment particle diameter and the Shields parameter. More recently, Khosravi et al. (2021) delved into the impact of non-uniform bed material as an additional influencing factor on sediment mobility during dam break flows. This is an area that calls for further in-depth research to enhance our understanding and provide a more comprehensive quantification of the relationship between suspended sediment near-bed concentration and substrate characteristics.

CONCLUSION

This study comprehensively investigated the influence of substrate level differences and material properties on dam break evolution over an erodible bed. The free surface advection was tracked using the VOF method coupled with non-equilibrium sediment flux in predicting scour, and van Rijn's (1984) bed load transport formula using a CFD package. Model validation was achieved by comparing the outcomes with previous studies on dam break over mobile beds (Leal et al., 2003, Spinewine and Capart, 2013). The ensuing key findings of this research are outlined below.

- The model demonstrated high predictive accuracy for both free surface evolution and substrate profiles, achieving NRMSE values of 0.042 and 0.205, respectively (Table 3). Additionally, the initial impact of substrate material and elevation disparity on flow velocity was minor. As substrate elevation differences decreased, flow velocity during wave evolution reduced, leading to dampened curvature in surface and substrate profiles and thinner sediment layers. Downstream, the lowest flow depth was near the dam, aligned with the most significant disturbance and substrate deformation at the greatest level difference. Reducing the level difference decreased the gap between the wavefront and downstream vertical and transverse velocities. Notably, the vertical velocity in the near field was roughly double the transverse velocity, offering an intriguing insight.
- The study provided insights into the Froude number (Fr), revealing an ascending pattern due to flow acceleration, albeit marked by fluctuations in the peak region due to intense turbulence. As the level difference decreased, the critical flow position shifted from the upstream region to the dam site. Decreases in level differences consistently led to lower Fr values, with greater disparities evident in the distinct sand characteristics of two reference experiments (Table 2). This emphasized the notable influence of the substrate on the prevailing flow regime throughout the downstream channel.
- An investigation into substrate roughness unveiled a transition from a smooth surface to an unstable configuration along the trajectory from the left wall toward

the near field. Notably, diminishing level differences precipitated a shift from a rough flow regimen to a transitional flow regimen. This transition was reflected in the concurrent decrease of Re_* values and highlighting the pivotal role played by the level difference in governing fluid dynamics.

- The patterns of air entrainment underwent substantial transformations during the initial phase. Commencing as bowl-shaped formations, they subsequently evolved into tongue-like structures beneath the advancing wavefront. The augmentation of air entrapment yielded an upward displacement of the wavefront's tip region, vividly illustrating the intricate interplay between air, water, and sediment dynamics.

In conclusion, this study provides invaluable insights into the intricate processes of erosion and sedimentation triggered by dam breaks. Initially, the reservoir substrate remained largely stationary due to the relatively low flow velocity. However, in subsequent stages, erosion became the dominant force shaping the substrate. Notably, the θ/θ_{cr} ratio decreased to about one-third, while the elevation difference increased fourfold. This research highlights the model's remarkable precision in evaluating dam failure scenarios, considering the complex interactions of erodible morpho-dynamic features. To enhance the model's applicability, future work could incorporate the intricate influences of non-uniform substrates, porosity, floodplains, bridges, and other river structures.

REFERENCES

Aleixo, R., Soares-Frazão, S., Zech, Y., 2010. Velocity profiles in dam-break flows: water and sediment layers. In: Proc. Int. Conf. on Fluvial Hydraulics "River Flow 2010", pp. 533–540.

An, S., Ku, H., Julien, P.Y., 2015. Numerical modelling of local scour caused by submerged jets. Maejo Int. J. Sci. Technol., 9, 3, 328–343.

Bahmanpouri, F., Daliri, M., Khoshkonesh, A., Namin, M.M., Buccino, M., 2021. Bed compaction effect on dam break flow over erodible bed; experimental and numerical modeling. J. Hydrol., 594, 125645. https://doi.org/10.1016/j.jhydrol.2020.125645

Baklanov, A., 2007. Environmental risk and assessment modelling – scientific needs and expected advancements. In: Ebel, A., Davitashvili, T. (Eds.): Air, Water and Soil Quality Modelling for Risk and Impact Assessment Springer, Dordrecht, pp. 29–44.

Biscarini, C., Di Francesco, S., Nardi, F., Manciola, P., 2013. Detailed simulation of complex hydraulic problems with macroscopic and mesoscopic mathematical methods. Math. Probl. Eng., 928309. https://doi.org/10.1155/2013/928309

Cao, Z., Pender, G., Wallis, S., Carling, P., 2004. Computational dam-break hydraulics over erodible sediment bed. J. Hydraul. Eng., 130, 7, 689–703.

Catucci, D., Briganti, R., Heller, V., 2021. Numerical validation of novel scaling laws for air entrainment in water. Proc. R. Soc. A, 477, 2255, 20210339. https://doi.org/10.1098/rspa.2021.0339

Dehrashid, F.A., Heidari, M., Rahimi, H., Khoshkonesh, A., Yuan, S., Tang, X., Lu, C., Wang, X., 2023. CFD modeling the flow dynamics in an open channel with double-layered vegetation. Model. Earth Syst. Environ., 9, 1, 543–555.

Desombre, J., Morichon, D., Mory, M., 2013. RANS v2-f simulation of a swash event: Detailed flow structure. Coastal Eng., 71, 1–12.

Dodangeh, E., Afzalimehr, H., 2022. Incipient motion of sediment particles in the presence of bed forms under decelerating and accelerating flows. J. Hydrol. Hydromech., 70, 1, 89–102.

Dong, Z., Wang, J., Vetsch, D.F., Boes, R.M., Tan, G., 2019. Numerical simulation of air entrainment on stepped spillways. In: E-proceedings of the 38th IAHR World Congress (pp. 1494). September 1–6, 2019, Panama City, Panama. DOI:

Alireza Khoshkonesh, Blaise Nsom, Saeid Okhravi, Fariba Ahmadi Dehrashid, Payam Heidarian, Silvia DiFrancesco

10.3850/38WC092019-0755

Flow3D [computer software]. 2023. Santa Fe, NM: Flow Science, Inc.

Fraccarollo, L., Capart, H., 2002. Riemann wave description of erosional dam-break flows. J. Fluid Mech., 461, 183–228.

Gu, Z., Wang, T., Meng, W., Yu, C.H., An, R., 2023. Numerical investigation of silted-up dam-break flow with different silted-up sediment heights. Water Supply, 23, 2, 599–614.

Gualtieri, P., De Felice, S., Pasquino, V., Doria, G.P., 2018. Use of conventional flow resistance equations and a model for the Nikuradse roughness in vegetated flows at high submergence. J. Hydrol. Hydromech., 66, 1, 107–120.

Heller, V., 2011. Scale effects in physical hydraulic engineering models. J. Hydraul. Res., 49, 3, 293–306.

Hirt, C.W., 2003. Modeling turbulent entrainment of air at a free surface. Flow Science, Inc.

Hirt, C.W., Nichols, B.D., 1981. Volume of fluid (VOF) method for the dynamics of free boundaries. J. Comput. Phys., 39, 1, 201–225.

Issakhov, A., Zhandaulet, Y., Nogaeva, A., 2018. Numerical simulation of dam break flow for various forms of the obstacle by VOF method. Int. J. Multiphase Flow, 109, 191–206.

Khayyer, A., Gotoh, H., 2010. On particle-based simulation of a dam break over a wet bed. J. Hydraul. Res., 48, 2, 238–249.

Khoshkonesh, A., Daliri, M., Riaz, K., Dehrashid, F.A., Bahmanpouri, F., Di Francesco, S., 2022. Dam-break flow dynamics over a stepped channel with vegetation. J. Hydrol., 613, 128395. https://doi.org/10.1016/j.jhydrol.2022.128395

Khoshkonesh, A., Nsom, B., Gohari, S., Banejad, H., 2019. A comprehensive study on dam-break flow over dry and wet beds. Ocean Eng., 188, 106279. https://doi.org/10.1016/j.oceaneng.2019.106279

Khoshkonesh, A., Sadeghi, S.H., Gohari, S., Karimpour, S., Oodi, S., Di Francesco, S., 2023. Study of dam-break flow over a vegetated channel with and without a drop. Water Resour. Manage., 37, 5, 2107–2123.

Khosravi, K., Chegini, A.H.N., Cooper, J., Mao, L., Habibnejad, M., Shahedi, K., Binns, A., 2021. A laboratory investigation of bed-load transport of gravel sediments under dam break flow. Int. J. Sediment Res., 36, 2, 229–234.

Kim, Y., Zhou, Z., Hsu, T.J., Puleo, J.A., 2017. Large eddy simulation of dam-break-driven swash on a rough-planar beach. J. Geophys. Res.: Oceans, 122, 2, 1274–1296.

Kocaman, S., Ozmen-Cagatay, H., 2012. The effect of lateral channel contraction on dam break flows: Laboratory experiment. J. Hydrol., 432, 145–153.

Leal, J.G., Ferreira, R.M., Cardoso, A.H., 2006. Dam-break wave-front celerity. J. Hydraul. Eng., 132, 1, 69–76.

Leal, J.G.A.B., Ferreira, R.M., Cardoso, A.H., 2003. Dam-break wave propagation over a cohesionless erodible bed. In: Proc. 30rd IAHR Congress, 100, 261–268.

Li, Y. L., Ma, Y., Deng, R., Jiang, D.P., Hu, Z., 2019. Research on dam-break induced tsunami bore acting on the triangular breakwater based on high order 3D CLSVOF-THINC/WLIC-IBM approaching. Ocean Eng., 182, 645–659.

Li, Y.L., Yu, C.H., 2019. Research on dam-break flow induced front wave impacting a vertical wall based on the CLSVOF and level set methods. Ocean Eng., 178, 442–462.

Mei, S., Chen, S., Zhong, Q., Shan, Y., 2022. Detailed numerical modeling for breach hydrograph and morphology evolution during landslide dam breaching. Landslides, 19, 12, 2925–2949.

Meng, W., Yu, C.H., Li, J., An, R., 2022. Three-dimensional simulation of silted-up dam-break flow striking a rigid structure. Ocean Eng., 261, 112042. https://doi.org/10.1016/j.oceaneng.2022.112042

Meyer-Peter, E., Müller, R., 1948. Formulas for bed-load transport. In: IAHSR 2nd meeting, Stockholm, appendix 2. IAHR.

Nielsen, P., 1984. Field measurements of time-averaged suspended sediment concentrations under waves. Coastal Eng., 8, 1, 51–72.

Nielsen, P., 2018. Bed shear stress, surface shape and velocity field near the tips of dam-breaks, tsunami and wave runup. Coastal Eng., 138, 126–131.

Nsom, B., Latrache, N., Ramifidisoa, L., Khoshkonesh, A., 2019. Analytical solution to the stability of gravity-driven stratified flow of two liquids over an inclined plane. In: 24th French Mechanics Congress in Brest. Brest, p. 244178.

Nsom, B., Ravelo, B., Ndong, W., 2008. Flow regimes in horizontal viscous dam-break flow of Cayous mud. Appl. Rheol., 18, 4, 43577-1. https://doi.org/10.1515/arh-2008-0012

Oguzhan, S., Aksoy, A.O., 2020. Experimental investigation of the effect of vegetation on dam break flood waves. J. Hydrol. Hydromech., 68, 3, 231–241.

Okhravi, S., Gohari, S., Alemi, M., Maia, R., 2022. Effects of bed-material gradation on clear water scour at single and group of piles. J. Hydrol. Hydromech., 70, 1, 114–127.

Okhravi, S., Gohari, S., Alemi, M., Maia, R., 2023. Numerical modeling of local scour of non-uniform graded sediment for two arrangements of pile groups. Int. J. Sediment Res., 38, 4, 597–614.

Parambath, A., 2010. Impact of tsunamis on near shore wind power units. Master's Thesis. Texas A&M University. Available electronically from https://hdl.handle.net/1969.1/ETD-TAMU-2010-12-8919

Pintado-Patiño, J.C., Puleo, J.A., Krafft, D., Torres-Freyermuth, A., 2021. Hydrodynamics and sediment transport under a dam-break-driven swash: An experimental study. Coastal Eng., 170, 103986. https://doi.org/10.1016/j.coastaleng.2021.103986

Riaz, K., Aslam, H.M.S., Yaseen, M.W., Ahmad, H.H., Khoshkonesh, A., Noshin, S., 2022. Flood frequency analysis and hydraulic design of bridge at Mashan on river Kunhar. Arch. Hydroengineering Environ. Mech., 69, 1, 1–12.

Ritter, A., 1892. Die Fortpflanzung der Wasserwellen. Zeitschrift des Vereines Deutscher Ingenieure, 36, 33, 947–954. (In German.)

Smagorinsky, J., 1963. General circulation experiments with the primitive equations: I. The basic experiment. Mon. Weather Rev., 91, 3, 99–164.

Soulsby, R.L., 1997. Dynamics of marine sands: a manual for practical applications. Oceanogr. Lit. Rev., 9, 44, 947.

Spinewine, B., Capart, H., 2013. Intense bed-load due to a sudden dam-break. J. Fluid Mech., 731, 579–614.

Van Rijn, L.C., 1984. Sediment transport, part I: bed load transport. J. Hydraul. Eng., 110, 10, 1431–1456.

Vosoughi, F., Rakhshandehroo, G., Nikoo, M.R., Sadegh, M., 2020. Experimental study and numerical verification of silted-up dam break. J. Hydrol., 590, 125267. https://doi.org/10.1016/j.jhydrol.2020.125267

Wu, W., Wang, S.S., 2008. One-dimensional explicit finite-volume model for sediment transport. J. Hydraul. Res., 46, 1, 87–98.

Xu, T., Huai, W., Liu, H., 2023. MPS-based simulation of dam-break wave propagation over wet beds with a sediment layer. Ocean Eng., 281, 115035. https://doi.org/10.1016/j.oceaneng.2023.115035

Yang, S., Yang, W., Qin, S., Li, Q., Yang, B., 2018. Numerical study on characteristics of dam-break wave. Ocean Eng., 159, 358–371.

Yao, G.F., 2004. Development of new pressure-velocity solvers in FLOW-3D. Flow Science, Inc., USA.